PHYSICAL REVIEW E **78**, 046712 (2008)

Improved path integration method for estimating the intrinsic viscosity of arbitrarily shaped particles

Marc L. Mansfield
Department of Chemistry and Chemical Biology, Stevens Institute of Technology, Hoboken, New Jersey 07030, USA

Jack F. Douglas
Polymers Division, National Institute of Standards and Technology, Gaithersburg, Maryland 20899, USA
(Received 12 May 2008; published 29 October 2008)

In previous work, we have established that the intrinsic viscosity $[\eta]$ of an object is nearly proportional to the average electrical polarizability tensor $\langle\boldsymbol{\alpha}_e\rangle=\mathrm{tr}(\boldsymbol{\alpha}_e)/3$ of a conducting object having the same shape, or equivalently, to the intrinsic conductivity $[\sigma]=\langle\boldsymbol{\alpha}_e\rangle/V$, which characterizes the conductivity of a dilute mixture of randomly oriented conducting objects (V being the volume of the object). This hydrodynamic-electrostatic analogy is useful because $\boldsymbol{\alpha}_e$ can be determined accurately and efficiently by numerical path integration for objects of arbitrary shape. Here, we show that the uncertainty in $[\eta]$ can be reduced to a relatively small value ($<1.5\%$ relative uncertainty) by utilizing additional information from the full tensor $\boldsymbol{\alpha}_e$, rather than just its average. Specifically, we determine the exact constant of proportionality between $[\eta]$ and $[\sigma]$ for triaxial ellipsoids as a function of the ratios of the eigenvalues of $\boldsymbol{\alpha}_e$ and apply this relation to particles of general shape. In addition to an improved estimation of $[\eta]$, the ratios of the components of $\boldsymbol{\alpha}_e$ provide useful measures of particle anisotropy. We also present an improved method for applying the technique to flexible particles, which requires performing a conformational ensemble average. Conformational averages of $\boldsymbol{\alpha}_e$ generate systematic errors that can be avoided by performing the conformational average at an earlier stage in the computation.

DOI: 10.1103/PhysRevE.78.046712 PACS number(s): 47.11.−j, 66.20.Cy

I. INTRODUCTION

A common approximation in hydrodynamic theory is to replace the Oseen tensor with its average over orientations, converting it to a scalar proportional to $1/r$ [1]. This has interesting implications since $1/r$ is the electrostatic Green's function. Specifically, boundary-value problems in hydrodynamics map directly to simpler boundary-value problems in electrostatics. We find, for example, that the distribution of Stokes force over the surface of a rigid body is approximately proportional to the charge distribution over the surface of a charged conductor having the same size and shape as the original body [2]. Furthermore, the hydrodynamic radius and the intrinsic viscosity are analogs, respectively, of the electrostatic capacity and the electrostatic polarizability of a perfect conductor having the same size and shape [2–11].

For a few simple shapes, e.g., ellipsoids, exact solutions to either the hydrodynamic or the electrostatic boundary-value problems are available [12]. However, for complex shapes, the traditional approach is finite-element numerical methods. In this category, we include surface-or boundary-element techniques [13–19], which tile the surface with small polygons, full volume-element methods [3,4], and computations based on point hydrodynamic sources ("beads") [20–28], which represent the surface with a large number of spherical beads. Such calculations require the numerical inversion of an $N_e\times N_e$ (for electrostatics problems) or of a $3N_e\times 3N_e$ (for hydrodynamics problems) matrix, for N_e the number of finite elements. Hence computation times scale as N_e^3. However, it has proven possible to obtain both the electrostatic capacity and the electrostatic polarizability tensor by a path-integration technique [2–10]. The path integrals can be evaluated for bodies of arbitrary complexity and are exact in the infinite sampling limit for both the capacity and the polarizability tensor. Furthermore, when the technique is applied to any equivalent finite-element model, integration time is proportional only to N_e, meaning that the technique is faster than the traditional approach for large N_e.

With the path integration providing highly accurate estimates of these electrostatic properties, we can then apply the hydrodynamic-electrostatic analogy to determine both the hydrodynamic radius and the intrinsic viscosity. Because the analogy is only approximate, determining the transport properties in this way induces uncertainty, currently at the level of 1% and 5%, respectively, for the hydrodynamic radius and the intrinsic viscosity [3,4,8–10]. The analysis involves the assumption that the particle is rigid, so to treat particles with conformational flexibility, we employ the Zimm rigid-body approximation [29], in which we average over the conformational ensemble. This paper has two main goals related to the determination of the intrinsic viscosity. First, the ensemble average required by the Zimm rigid-body approximation involves certain subtleties, so below we explain the appropriate procedure. Second, we describe a refinement to our former procedure that decreases the uncertainty in the intrinsic viscosity from 5% to apparently about 1.5% or less for many bodies. The determination of the hydrodynamic radius, which parallels the intrinsic viscosity calculation and which has always been more accurate, is not being modified here. Indeed the hydrodynamic-electrostatic analogy is exact for the hydrodynamic radius of triaxial ellipsoids, and the refinement reported here ensures the same for the intrinsic viscosity of ellipsoids.

First, we define several quantities essential to our development. The electrostatic capacity, C, of a perfect conductor is the proportionality constant between applied electric charge and induced electrostatic potential, and has the units of length. The electrostatic polarizability tensor, $\boldsymbol{\alpha}_e$, is the proportionality constant between applied external field and induced dipole moment, and has units of volume. The intrinsic conductivity, $[\sigma]$, is the leading virial coefficient for the conductivity of an inclusion of conducting particles in an insulating medium, and obeys [3,4]

$$[\sigma] = \frac{\langle \boldsymbol{\alpha}_e \rangle}{V}, \tag{1}$$

where

$$\langle \boldsymbol{\alpha}_e \rangle = \frac{1}{3} \sum \alpha_{ii} \tag{2}$$

is the mean polarizability, and where V is the particle volume. Furthermore, $[\sigma]$ is a dimensionless, scale-invariant shape functional. The hydrodynamic radius, R_h, is the proportionality constant between the friction coefficient and the solvent viscosity,

$$f = 6\pi\eta R_h, \tag{3a}$$

and has units of length. It is also directly connected to the diffusivity,

$$D = \frac{kT}{f} = \frac{kT}{6\pi\eta R_h}. \tag{3b}$$

The intrinsic viscosity, $[\eta]$, is the second virial coefficient of the viscosity of a solution, and is also a dimensionless, scale-invariant shape functional. (The "practical" intrinsic viscosity, as used in most experimental work, is $[\eta]_P = V[\eta]/m$, m is the mass of the body.)

In Sec. II, we describe the technique for performing conformational ensemble averages of the polarizability. In Sec. III, we review current approaches for inferring the intrinsic viscosity from the polarizability. In Sec. IV, we present our refined approach, and in Sec. V, we present tests of its accuracy. Section VI gives a summary and some conclusions.

II. ADAPTATIONS FOR ENSEMBLE AVERAGES OF THE POLARIZABILITY

In a study applying our computational method to a wormlike chain model [30], we became aware of certain subtleties involved in taking conformational ensemble averages of the polarizability. It turns out that a simple arithmetic mean of the polarizability over conformations gives incorrect results. To explain the correct way to perform such averages, we find it necessary to describe here the complete path-integration technique in some detail. However, we include justification only of those steps that have never been described in the literature and refer the reader to the literature for additional justifications [2–10].

The body (polymer, nanoparticle, etc.) to be examined by the path-integration algorithm is circumscribed by a sphere, the so-called launch sphere. (See Fig. 2 of [8].) Any sphere that circumscribes the body is acceptable, although we achieve better sampling statistics if we use smaller launch spheres. Let R denote the radius of the launch sphere. We employ a Cartesian coordinate system with the origin at the center of this sphere. We select at random some point $\boldsymbol{x}_i = (x_{i1}, x_{i2}, x_{i3})$, where the subscript "$i$" denotes that this is the initiation point of a random walker. Three separate "charges" are then assigned at random to this point depending on its position on the sphere. The charge c_1 is taken to be $+1$ with probability $\frac{1}{2}(1+\frac{x_{i1}}{R})$, otherwise, it is taken to be -1. Charges c_2 and c_3 are determined in an equivalent manner from x_{i2} and x_{i3}, respectively. A random walker is initiated from this point on the sphere, and a representative trajectory is generated until the walker either makes first passage to the surface of the body at the final point $\boldsymbol{x}_f = (x_{f1}, x_{f2}, x_{f3})$ or until it "escapes to infinity" (a finite fraction of all random walkers never make first passage to the surface, even after infinite time). We refer the reader to our previous publications for a description of the methods we use to generate these trajectories [8–10]. This procedure is repeated a total of N times, where N is taken as large as possible to minimize sampling error. Let K_j^+, $j=1,2,3$, be the number of trajectories possessing charge $c_j = +1$ that adsorb on the body, and let K_j^- be the number of trajectories possessing charge $c_j = -1$ that adsorb. Furthermore, let

$$(V_{j1}^+, V_{j2}^+, V_{j3}^+) = \sum_{c_j=+1} (x_{f1}, x_{f2}, x_{f3}) \tag{4a}$$

and

$$(V_{j1}^-, V_{j2}^-, V_{j3}^-) = \sum_{c_j=-1} (x_{f1}, x_{f2}, x_{f3}) \tag{4b}$$

be the vector sums of all the termination points of all walkers for which $c_j = +1$ or $c_j = -1$, respectively. We also let

$$t = \frac{K_1^+ + K_1^-}{N} = \frac{K_2^+ + K_2^-}{N} = \frac{K_3^+ + K_3^-}{N} \tag{5}$$

be the fraction of random walkers that adsorb (as opposed to escaping to infinity), and we let

$$u_j = \frac{K_j^+ - K_j^-}{N}, \tag{6a}$$

$$v_{ij} = \frac{V_{ij}^+ + V_{ij}^-}{N}, \tag{6b}$$

$$w_{ij} = \frac{V_{ij}^+ - V_{ij}^-}{N}. \tag{6c}$$

Then the capacity and polarizability tensor are given by

$$C = tR, \tag{7a}$$

$$(\boldsymbol{\alpha}_e)_{ij} = 12\pi R^2 \left(w_{ij} - \frac{u_j v_{ij}}{t} \right), \tag{7b}$$

Eqs. (6) and (7) are exact in the infinite-sampling limit.

Consider now the problem of combining the results of two or more independent integrations on the same body. Since any trajectory is independent of any other, two integrations, each sampling N trajectories, are equivalent to a single integration sampling $2N$ trajectories. Of course, it is tempting to combine two or more such integrations by taking a simple arithmetic mean:

$$C = \langle t \rangle R, \tag{8}$$

$$(\boldsymbol{\alpha}_e)_{ij} = 12\pi R^2 \left\langle w_{ij} - \frac{u_j v_{ij}}{t} \right\rangle, \tag{9}$$

where the angle brackets represent an average over two or more independent integrations. Equation (8) is correct for the capacity, but it is not difficult to show that the correct combining rule for the polarizability is

$$(\boldsymbol{\alpha}_e)_{ij} = 12\pi R^2 \left[\langle w_{ij} \rangle - \frac{\langle u_j \rangle \langle v_{ij} \rangle}{\langle t \rangle} \right] \tag{10}$$

rather than Eq. (9).

Assume now that we are examining a body with conformational flexibility. In this case, we generate m objects, each one a representative of the conformational ensemble of the particle. For rigid bodies, $m=1$, but for nonrigid bodies, we want to take m as large as practical. As already stated, we employ the "Zimm rigid-body approximation" in this case [29]. In this approximation, we treat each of the m members of the conformational ensemble as a rigid body, compute its transport properties, and take an ensemble average over all m bodies at the end. Furthermore, we take Eqs. (8) and (10) as the proper ensemble average over conformations, rather than Eq. (9), with the added precaution of using the same launch sphere for all elements of the ensemble and launching the same number of trajectories for each element of the ensemble. (To do otherwise would be tantamount to giving different weights to different elements of the ensemble.)

The argument for using Eq. (10) rather than Eq. (9) is straightforward for the problem of combining independent runs on identical models. The ultimate justification for using it with conformational averages as well is that only Eq. (10) is valid in the limit that all conformations converge on any given conformation, one example being the wormlike chain in the rod limit.

The distinction between the two averages, Eqs. (9) and (10), becomes small in the limit of large N. In other words, Eq. (9) engenders systematic sampling errors that can be avoided either by using sufficiently large N or by using Eq. (10) [31]. However, for any given ensemble average, we must generate N trajectories for each of m different conformations, and it is impossible, with current technology, to employ N large enough that Eq. (9) becomes adequate. For example, in most of our work, we take Nm on the order of 10^6 or 10^7. If we then take $m=10^3$, this leaves N in the range of 10^3 or 10^4. We are reasonably confident that 10^6-10^7 samples of any one ensemble is adequate for accurate ensemble averages, but this is only true if we use Eq. (10) rather than Eq. (9). In our work on wormlike chains, for example, we have found that the two approaches can differ by as much as about 10% near the rod limit [30].

III. HYDRODYNAMIC-ELECTROSTATIC ANALOGY AND THE ESTIMATE OF INTRINSIC VISCOSITY

The relation between the hydrodynamic radius, R_h, and the electrostatic capacity, C, of particles of general shape was first observed by Douglas, based on the Kirkwood-Riseman theory of polymer hydrodynamics. (See Ref. [11] for a discussion.) Later, Hubbard and Douglas [2] made formal arguments that R_h equals C *exactly* for arbitrary shaped objects, not just slender bodies such as polymers. They noted that this relation is exact for any triaxial ellipsoid, thereby recovering the well-known Perrin formulas [32]. They also provided much computational and experimental data that were consistent with $R_h=C$ to within uncertainties in computation or measurement. Since that time, however, additional data have accumulated that indicate that the relation is only approximate, although the discrepancy (usually 1% or less in cases where precise comparisons can be made) is below experimental measurement uncertainties. Therefore, we write

$$R_h = q_h C, \tag{11}$$

where q_h, a functional of the particle shape, is always near unity:

$$q_h = 1.00 \pm 0.01. \tag{12}$$

Douglas and Garboczi extended this argument by pointing out a similar proportionality between the intrinsic viscosity, $[\eta]$, and the intrinsic conductivity, $[\sigma]$, of arbitrarily shaped objects [3]:

$$[\eta] = q_\eta [\sigma] = \frac{q_\eta \langle \boldsymbol{\alpha}_e \rangle}{V}. \tag{13}$$

(This relation is a clear analog of the exact proportionality between the virtual mass and the magnetic polarizability tensor of a conductor of arbitrary shape [3].) Equivalently, we also have

$$[\eta]_P = \frac{q_\eta \langle \boldsymbol{\alpha}_e \rangle}{m} \tag{14}$$

for the practical intrinsic viscosity. Douglas and Garboczi fixed q_η for d-dimensional spheres ($d \geqslant 2$), where it is exactly

$$q_\eta = \frac{d+2}{2d}, \tag{15}$$

although they realized that q_η was not entirely independent of shape. When $d=3$, Eq. (15) yields the classical Einstein-Maxwell result of $5/6=0.833\ldots$. Exact results for several other bodies in three dimensions make it clear that this estimate of q_η is not exact [3]. For example, $q_\eta=4/5$ exactly for infinitely long rods, infinitely long prolate ellipsoids of revolution, and circular plates, and $q_\eta=3/4$ for a pair of spheres (dumbbell) in the limit of infinite separation. [See also Eq. (A1) [33].] Clearly, the ratio $[\eta]/[\sigma]$ varies slowly with variation in particle shape. A survey [3] of a wide variety of exact and finite-element estimates for many bodies places q_η in the interval,

$$q_\eta = 0.79 \pm 0.04. \tag{16}$$

These hydrodynamic-electrostatic analogies are extremely useful since efficient numerical path integration methods are available that compute both C and $\boldsymbol{\alpha}_e$ of arbitrarily shaped objects [5–10], thereby allowing estimates of R_h and $[\eta]$ with prescribed uncertainties that are comparable to experimental uncertainties.

In this paper, we obtain an improved estimate of the virial ratio q_η. This improvement is based on the assumption that the complete polarizability tensor $\boldsymbol{\alpha}_e$ carries enough information about the shape of the object to permit a more accurate estimation of q_η. The improved technique, explained in the following section, is based on the simple idea of demanding that the q_η in Eq. (14) be exact for triaxial ellipsoids, and then by assuming that the same q_η can be applied to any object having the same polarizability tensor.

IV. INTRINSIC VISCOSITY -INTRINSIC CONDUCTIVITY PREFACTOR FOR ELLIPSOIDS

As a rank-2 symmetric tensor, the polarizability carries no more rotationally invariant information about the body than the values of its three eigenvalues: $\alpha_1 \leq \alpha_2 \leq \alpha_3$. Furthermore, since q_η is scale-invariant, we only need to consider two ratios of the three eigenvalues: α_2/α_1 and α_3/α_2, for example, to characterize the average particle "anisotropy." In other words, the polarizability tensor provides a mapping to a two-dimensional "shape space" that we expect should also be useful for particle shape classification. We then need to devise a mapping from this shape space to values of q_η. To calibrate the mapping, we will use the one class of shapes which completely cover the shape space and for which the α_i, $[\sigma]$, and $[\eta]$ can all be accurately calculated, the ellipsoids [3,12]. The calibration as afforded by the ellipsoids is presented in this section. Then, in Sec. V, we test our predictions of q_η based on this approach for a number of shapes for which accurate independent results are available.

We let a_i represent the three semiaxes of an arbitrary ellipsoid, and assume that they are labeled such that $a_1 \leq a_2 \leq a_3$. From these, we can calculate each α_i, the three diagonal components of the polarizability tensor $\boldsymbol{\alpha}_e$ [3,12] and we assume that these are also ordered: $\alpha_1 \leq \alpha_2 \leq \alpha_3$. We can also calculate $[\sigma]$, $[\eta]$, and therefore q_η [3,12]. However, the computation is not trivial. To map from the eigenvalues α_i to q_η would require solving a two-dimensional parametric equation involving numerical evaluation of elliptic integrals. Our approach, therefore, is to design a Padé approximant that determines q_η quickly and directly from the eigenvalues of the polarizability.

As already mentioned, the shape space is two-dimensional, and we have chosen the two coordinates

$$x_1 = \ln\left(\frac{\alpha_2}{\alpha_1}\right) \tag{17a}$$

and

$$x_2 = \ln\left(\frac{\alpha_3}{\alpha_2}\right) \tag{17b}$$

as independent variables that characterize the "polarizability ellipsoid" [34]. To describe the physical ellipsoid, we use the variables

$$z_1 = \ln\left(\frac{a_2}{a_1}\right) \tag{18a}$$

and

$$z_2 = \ln\left(\frac{a_3}{a_2}\right). \tag{18b}$$

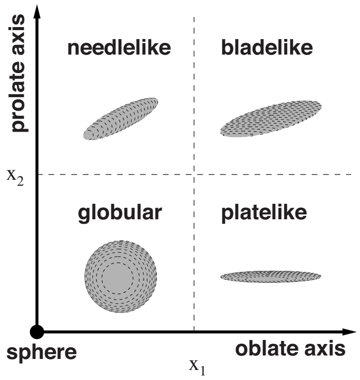

FIG. 1. The polarizability ellipsoid of any object is mapped to a point in a two-dimensional shape space described by the two coordinates x_1 and x_2. The sphere maps to the origin, all oblate ellipsoids of revolution map to the x_1 axis, while all prolate ellipsoids of revolution map to the x_2 axis. If x_1 and x_2 are both small, the ellipsoid is globular. If one is large while the other is small, the ellipsoid is either platelike or needlelike. If both are large, the ellipsoid is bladelike, i.e., it has a large aspect ratio in three dimensions, but its two-dimensional cross section itself has a large aspect ratio.

Obviously, the polarizability ellipsoid at the point $(x_1,x_2)=(0,0)$ is the sphere. Points along the axis $(x_1,0)$, where $\alpha_1 < \alpha_2 = \alpha_3$, represent the oblate ellipsoids of revolution, and $(x_1 \to \infty, 0)$ represents the limit of a circular disk. Points along the axis $(0,x_2)$, where $\alpha_1 = \alpha_2 < \alpha_3$ represent the prolate ellipsoids of revolution, and the limit $(0, x_2 \to \infty)$ represent needlelike ellipsoids of revolution. The best way to conceive of the polarizability ellipsoid at an arbitrary point (x_1,x_2) is the following. Start at the point (0, 0) representing a sphere. Distort the sphere into an oblate ellipsoid of revolution by moving to the point $(x_1,0)$. Then distort that ellipsoid by stretching it in a direction orthogonal to its axis until the point (x_1,x_2) is reached. We can think of x_2 as representing the logarithm of the aspect ratio of the final ellipsoid, and x_1 as representing the logarithm of the aspect ratio of its elliptical cross section. As we move in the direction $x_1 \to \infty$, the object becomes quasi-two-dimensional; as we move in the direction $x_2 \to \infty$, it becomes quasi-one-dimensional. Figure 1 summarizes the relationship between points in shape space and the configuration of the polarizability ellipsoid.

TABLE I. Coefficients of the Padé approximant, Eq. (20).

	$i=1$	$i=2$	$i=3$	$i=4$
δ_i	4.8	0.66	−1.247	0.787
k_i	0	1.04	2.012	2.315
b_i	0.68	−7.399	1.048	0.136
t_i	0	1.063	0.895	4.993
B_i	1.925	−8.611	1.652	−0.120
q_i	0	1.344	2.029	1.075
c_i	13.43	16.17	0.51	−5.86
r_i	0	0.489	0.879	2.447
A_i	16.23	−15.92	14.83	−3.74
v_i	0	0.462	1.989	4.60
m_i	2.786	0.293	−0.11	0.012
u_i	0	0.556	2.034	3.024

We have constructed the Padé approximant to take the form

$$q_\eta(x_1,x_2) = \frac{\delta A + c x_2 + b x_2^2 + 4 x_2^m}{6A + \dfrac{6 c x_2}{\delta} + B x_2^2 + 5 x_2^m}, \tag{19}$$

where δ, A, c, b, B, and m are the following functions of x_1:

$$\delta = \sum_{i=1}^{4} \delta_i \exp(-k_i x_1), \tag{20a}$$

$$b = \sum_{i=1}^{4} b_i \exp(-t_i x_1), \tag{20b}$$

$$B = \sum_{i=1}^{4} B_i \exp(-q_i x_1), \tag{20c}$$

$$c = \sum_{i=1}^{4} c_i \exp(-r_i x_1), \tag{20d}$$

$$A = \sum_{i=1}^{4} A_i \exp(-v_i x_1), \tag{20e}$$

$$m = \sum_{i=1}^{4} m_i \exp(-u_i x_1). \tag{20f}$$

The coefficients were determined by simulated annealing and are given in Table I. In the Appendix, we motivate this choice of the approximant.

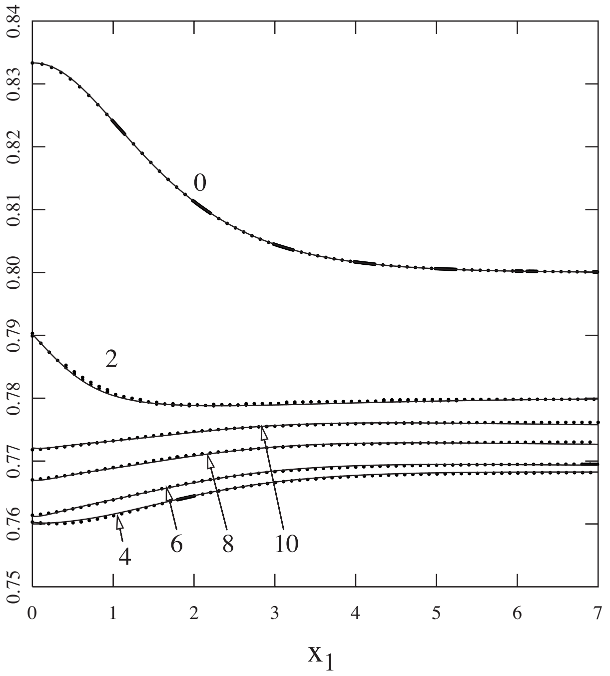

FIG. 2. Virial ratio q_η as a function of x_1 at various values of x_2. Symbols show the exact, numerical results, while the solid curves are calculated using the Padé approximant. Each curve is labeled with the value of x_2 at which it has been calculated.

Figures 2 and 3 compare exact results for q_η with those of the Padé approximant. We can see that the approximant gives three- to four-figure accuracy or better. Only data in the range $x_1 \in [0,7]$, $x_2 \in [0,12]$ were employed in constructing the approximant. However, as can be seen in Fig. 2, q_η is effectively independent of x_1 beyond $x_1=7$ (the body is then effectively two-dimensional) and to reflect this behavior the approximant has been designed to become independent of x_1 for x_1 sufficiently large. We therefore believe that the approx-

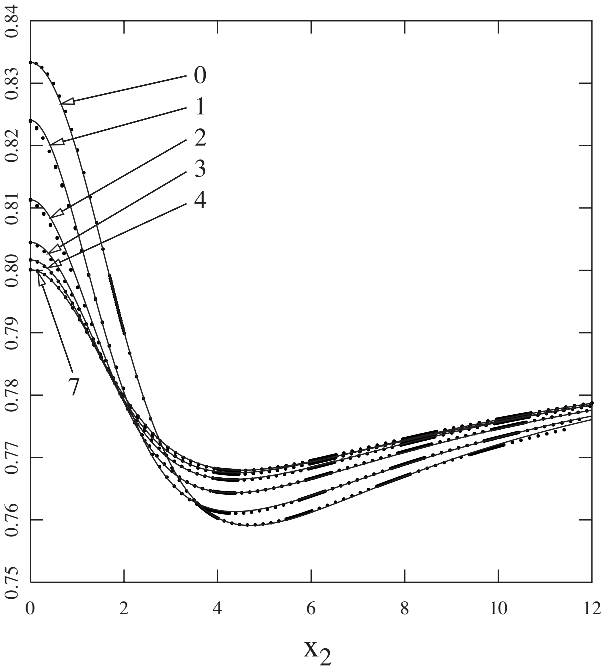

FIG. 3. Virial ratio q_η as a function of x_2 at various values of x_1. Symbols show the exact, numerical results, while the solid curves are calculated using the Pad é approximant. Each curve is labeled with the value of x_1 at which it has been calculated.

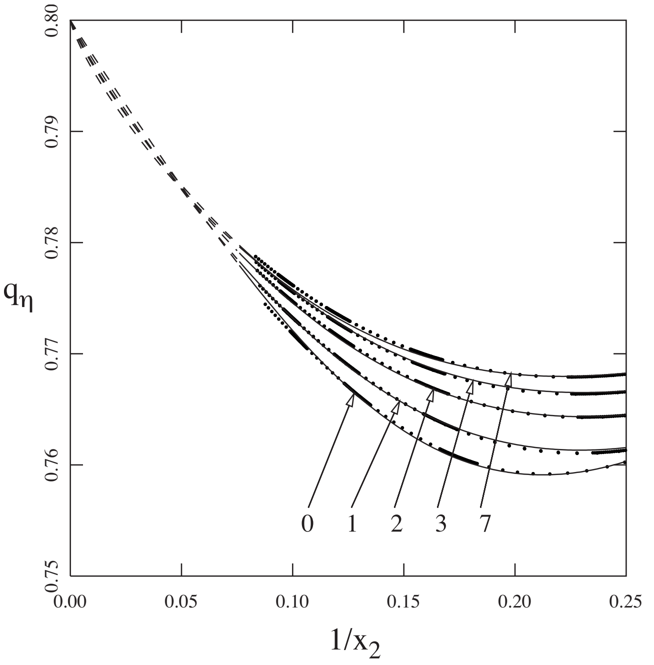

FIG. 4. Virial ratio q_η as a function of x_2^{-1} at various values of x_1. Symbols show the exact, numerical results, the solid and the dashed curves show the Padé approximant at $x_2 < 12$ and $x_2 > 12$, respectively. Each curve is labeled with the value of x_1 at which it has been calculated.

imant can be trusted in regions of shape space $x_1 > 7$. By contrast, convergence to the $x_2 \to \infty$ limit is much slower. Figure 4 shows how the Padé approximant behaves as a function of $1/x_2$ as x_2 grows without bound. Even though the approximant has been designed to reproduce the exact ellipsoid result $q_\eta(x_1,\infty) = 4/5$, Fig. 4 demonstrates that convergence to the limit is very slow and that interpolations between $x_2 = 12$ and ∞ might not be extremely accurate. However, we doubt that any bodies with aspect ratios greater than e^{12} are mechanically stable and therefore believe that the Padé approximant is sufficient to describe any physically realistic particle. Figure 5 is a contour plot that shows how $q_\eta(x_1,x_2)$ (calculated by the Padé approximant) varies throughout shape space.

To infer $[\eta]$ for an arbitrary shape, we first determine its polarizability tensor as explained in Sec. II, and then determine its eigenvalues [35]. Using Eqs. (17a), (17b), (19), and (20), we can estimate q_η for the object. Finally, Eq. (13) or Eq. (14) gives us the intrinsic viscosity. For particles with conformational flexibility, we propose extending Eq. (10) to read

$$[\eta] = \frac{4\pi R^2}{V} \sum_i \left[\langle q_\eta(x_1,x_2) w_{ii} \rangle - \frac{\langle u_i \rangle \langle q_\eta(x_1,x_2) v_{ii} \rangle}{\langle t \rangle} \right]. \tag{21}$$

In the above, the angle brackets denote a conformational average, and each $q_\eta(x_1,x_2)$ represents the Padé approximant evaluated for any one conformation.

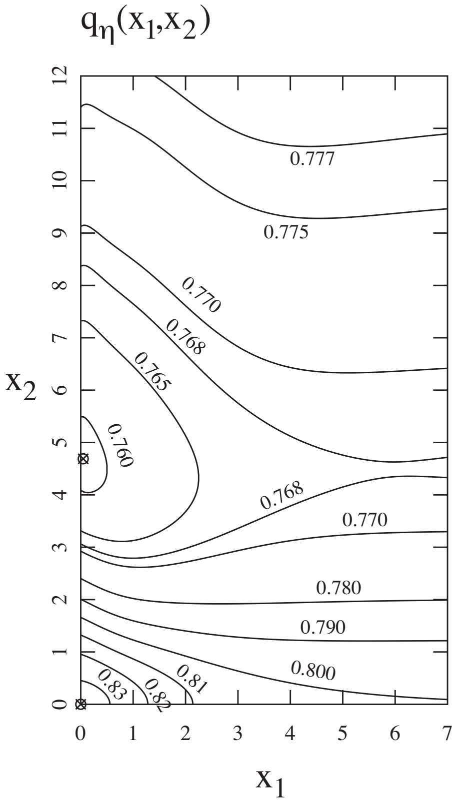

FIG. 5. Contour plot for the variation of $q_\eta(x_1,x_2)$ as a function of x_1 and x_2. The global maximum and minimum occur at $q_\eta(0,0) = 0.833\ldots$ and $q_\eta(0.047, 4.689) = 0.759$, respectively.

V. COMPARISONS WITH OTHER CALCULATIONS

By construction, the approach described above for the estimation of $[\eta]$ from $\boldsymbol{\alpha}_e$ is exact for ellipsoids, at least to within the fitting uncertainty of the Padé approximant. To test it for other bodies, we need accurate, independent determinations of both $[\eta]$ and $[\sigma]$. Table II displays such data from a number of sources. The sphere and the disk are special cases of ellipsoids; the exact, known results reported here are taken from Ref. [3] Dumbbells, i.e., two disjoint spheres regarded as a single body, are also amenable to exact calculation [3,36,37]. Each dumbbell is characterized by the quantity r_p, the ratio of the sphere separation to the sphere diameter, and results for several different dumbbells are given in Table II [38]. Aragon and Hahn (AH) [18,39] have computed both $[\eta]$ and $[\sigma]$ by boundary elements for the five Platonic solids and for several cylinders. Douglas and Garboczi (DG) [3] have computed $[\sigma]$ and $[\eta]$ by finite elements for a number of different shapes ("sponges," cylinders, prisms, a "jack," a pair of "dice," and the square; see their paper for precise specifications of these shapes).

Our previous paper [8] focused on the relationship between $[\eta]$ and $[\sigma]$ for many of the same shapes. We now reconsider this relationship in the light of more recent data and of our newer technique. For the same shapes, we have performed path integrations of $\boldsymbol{\alpha}_e$ and calculated q_η using the Padé approximant given above. Our results appear in Figs. 6 and 7 and in Table II. Figure 6 gives $[\eta]_{pi}$ as a function of $[\sigma]_{pi}$ for each of the shapes, with the subscript "*pi*" denoting

TABLE II. Comparison with other calculations. Each digit enclosed in parentheses in column 3 gives the sampling uncertainty in the last displayed digit.

Shape	$[\sigma]_{id}$	$[\sigma]_{pi}$	$[\sigma]_{id}/[\sigma]_{pi}$	$q_{\eta,id}$	$q_{\eta,\mathrm{Pade}}$
Exact results					
Sphere	3	2.997(2)	1.00	5/6	0.833
Disk,[a] radius r	$32r/9\pi t$	$\frac{[1.1310(6)]r}{t}$	1.00	4/5	0.800
Dumbbell (1)	4.2072	4.207(2)	1.00	0.820	0.819
Dumbbell (1.0201)	4.2702	4.277(3)	1.00	0.819	0.819
Dumbbell (1.1276) [38]	4.6180	4.618(3)	1.00	0.796	0.816
Dumbbell (1.5431)	6.0912	6.088(4)	1.00	0.803	0.806
Dumbbell (3.7622)	19.176	19.17(2)	1.00	0.770	0.771
Dumbbell (6.1323)	43.856	43.85(3)	1.00	0.759	0.762
Dumbbell (10.0677)	109.603	109.64(7)	1.00	0.754	0.759
Dumbbell (∞)	r_p^2	$[1.005(2)]r_p^2$	1.00	3/4	0.800 [Eq. (A1)]
Platonic solids computed by boundary elements [18]					
Tetrahedron	5.064	5.029(1)	1.007	0.831	0.833
Cube	3.667	3.6437(6)	1.006	0.845	0.833
Octahedron	3.572	3.5509(2)	1.006	0.844	0.833
Dodecahedron	3.196	3.1779(3)	1.006	0.842	0.833
Icosahedron	3.144	3.1305(4)	1.004	0.838	0.833
Cylinders computed by boundary elements [39]					
Cylinder ($d/h=0.4$)	4.632	4.631(4)	1.000	0.822	0.811
Cylinder ($d/h=0.2$)	8.087	8.091(9)	0.999	0.793	0.786
Cylinder ($d/h=0.133_{\ldots}$)	12.573	12.61(2)	0.997	0.779	0.773
Cylinder ($d/h=0.1$)	17.935	17.92(3)	1.001	0.771	0.767
Computed by finite elements [3]					
Sponge, 15/27	8.74	8.495(4)	1.03	0.819	0.833
Sponge, 21/27	27.1	26.31(1)	1.03	0.812	0.833
Sponge, 23/27	55.0	53.32(3)	1.03	0.813	0.833
Sponge, 25/27	192	184.2(1)	1.04	0.812	0.833
Sponge, 33/35	311	294.4(2)	1.06	0.820	0.833
Cylinder ($d/h=0.5$)	4.32	4.111(2)	1.05	0.799	0.819
Cylinder ($d/h=1$)	3.56	3.402(1)	1.05	0.815	0.833
Cylinder ($d/h=2$)	3.79	3.621(1)	1.05	0.813	0.830
Cylinder ($d/h=4$)	4.93	4.706(2)	1.05	0.797	0.820
Cube	3.72	3.6437(6)	1.02	0.820	0.833
Prism (2 × 1), prolate	4.22	4.143(2)	1.02	0.808	0.824
Prism (3 × 1), prolate	5.21	5.079(3)	1.03	0.793	0.811
Prism (4 × 1), prolate	6.38	6.210(5)	1.03	0.781	0.800
Prism (5 × 1), prolate	7.72	7.509(6)	1.03	0.772	0.792
Prism (10 × 1), prolate	16.4	15.86(2)	1.03	0.750	0.770
Prism (1 × 2), oblate	4.15	4.071(2)	1.02	0.810	0.828
Prism (1 × 3), oblate	4.84	4.749(2)	1.02	0.802	0.822
Prism (1 × 4), oblate	5.58	5.465(3)	1.02	0.800	0.818
Prism (1 × 5), oblate	6.34	6.198(4)	1.02	0.792	0.815
Prism (1 × 10), oblate	10.2	9.884(8)	1.03	0.776	0.808
Jack	4.50	4.258(2)	1.06	0.818	0.833
Dice	7.44	7.247(4)	1.03	0.785	0.807

TABLE II. (*Continued.*)

Shape	$[\sigma]_{id}$	$[\sigma]_{pi}$	$[\sigma]_{id}/[\sigma]_{pi}$	$q_{\eta,id}$	$q_{\eta,\mathrm{Pade}}$
Square,[a] side a	$0.73(\frac{a}{t})$	$[0.6931(6)]a/t$	1.05	0.77	0.800

[a] $[\sigma]$ and $[\eta]$ diverge for two-dimensional shapes such as the disk or the square, since they have zero volume. For the purposes of this table, we assume that such shapes have infinitesimal thickness t, so that $[\sigma]$ and $[\eta]$ both exist, both diverge like $1/t$, and their ratio tends to a well-defined finite limit.

"path integration." The range of $[\eta]$ in this figure extends from 2.5 to about 10^3. The solid line indicates $q_\eta=0.79$, the proportionality factor estimated in previous work [4,8]. Dotted lines show the uncertainty interval found previously, $q_\eta=0.79\pm0.04$. Although the uncertainty estimates in $[\eta]$ appear small on the logarithmic scale of Fig. 6, the deviations are real and larger than optimal for precise characterization work. Column 2 of Table II lists $[\sigma]_{id}$, or values of $[\sigma]$ extracted from the literature, with the subscript "*id*" signifying "independent determination." Column 3 lists $[\sigma]_{pi}$, which provides an independent check of the boundary-or finite-element results, and column 4 gives the ratio $[\sigma]_{id}/[\sigma]_{pi}$. Notice that $[\sigma]_{id}/[\sigma]_{pi}$ is very near 1 in all cases for which $[\sigma]$ and $[\eta]$ can be determined exactly, which is a verification of the path integration approach. Whenever $[\sigma]_{id}/[\sigma]_{pi}$ is much different from 1, we are justified in being suspicious of the independent calculation because the $[\sigma]_{pi}$ result is exact up to sampling error. This ratio is within a single percentage point of unity for the platonic solids as calculated by AH and for the cylinders as calculated by Aragon, but the deviations are several percent for the calculations of DG. This indicates a shortcoming of the finite-element technique: Large numbers of elements are needed for high accuracy, and convergence can be slow. (This shortcoming was appreciated by Douglas and Garboczi.) It also indicates that of the two classes of studies, the AH boundary-element computations seem to be more accurate.

In the interest of conserving space, we have not tabulated $[\eta]_{id}$ here, but column 5 of Table II records independently reported estimates of $q_{\eta,id}=[\eta]_{id}/[\sigma]_{id}$. Column 6 summarizes $q_{\eta,\mathrm{Pade}}$ values obtained for each of the shapes using the Padé approximant. If our procedure for inferring $q_{\eta,\mathrm{Pade}}$ is

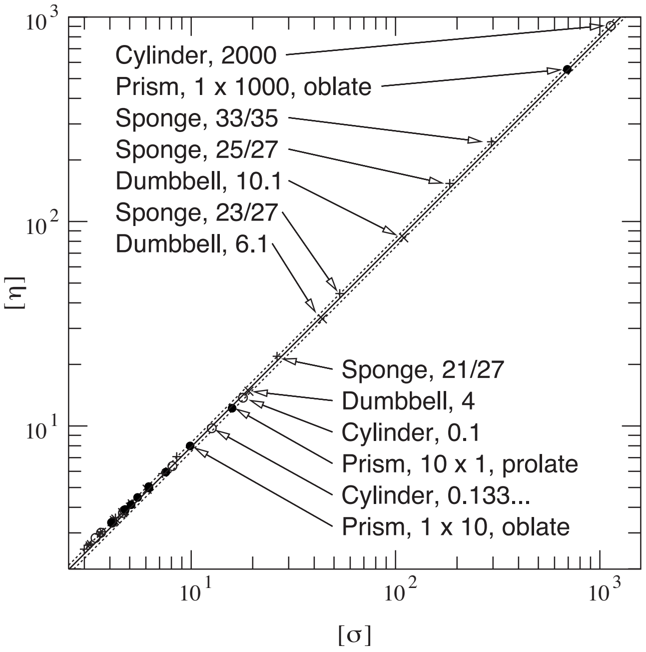

FIG. 6. Comparison between the path integration results for $[\sigma]$ and $[\eta]$ as computed for various bodies. The solid line and two dashed lines represent $q_\eta=0.79\pm0.04$. Results for dumbbells (○), platonic solids (*), cylinders (×), prisms (●), and various other bodies (+) are shown. The shape corresponding to any given point is also indicated whenever $[\eta]>10$. The diameter-to-height ratio is shown for cylinders, the ratio of sphere separation to sphere diameter is shown for dumbbells, the height and width are shown for prisms. See Ref. [3] for the definition and size specification of sponges.

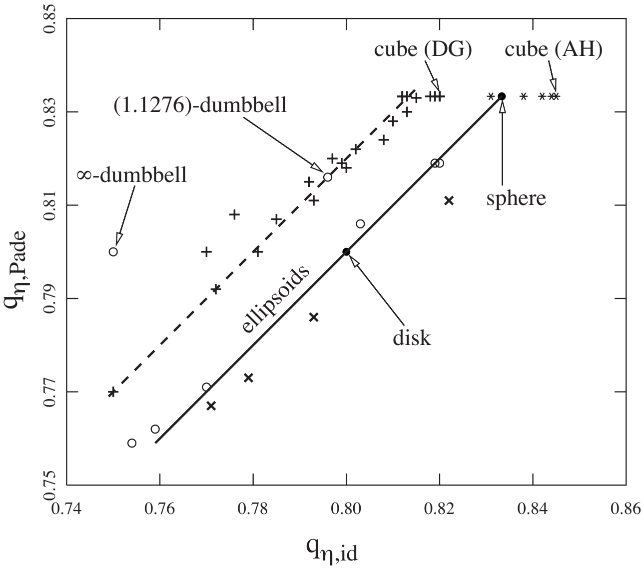

FIG. 7. Comparison between our approximations for the q_η ratio ($q_{\eta,\mathrm{Pade}}$) and those of independent determinations ($q_{\eta,id}$). All ellipsoids (including the sphere and the disk) fall on the solid line $q_{\eta,\mathrm{Pade}}=q_{\eta,id}$. Exact results for dumbbells (○) [3], boundary-element results for the five platonic solids (*) [18], boundary-element results for cylinders (×) [39], and finite-element results for various bodies (+) are shown [3]. Points corresponding to two different independent computations on the cube and to the dumbbells at separations of both 1.128 and ∞ are indicated. The finite-element data from Ref. [3] all cluster around the dashed line $q_{\eta,\mathrm{Pade}}=q_{\eta,id}+0.020$.

accurate, and if the $q_{\eta,id}$ values can all be trusted, then we should expect good agreement between columns 5 and 6. A graphical comparison appears in Fig. 7. The solid line indicates $q_{\eta,\mathrm{Pade}}=q_{\eta,id}$, which as explained above, is exact for all ellipsoids. The two degenerate ellipsoids, the sphere and the disk, fall on the line at the indicated points. As anticipated from the discussion above, the finite-element data lie systematically above the curve for ellipsoids, while the boundary-element calculations lie slightly below. This figure also includes data for separated dumbbells and indicates that the approach apparently becomes problematic in the (unphysical) case of particles that are not simply connected [38]. All five platonic solids [18,19,40] and the cylinders [39] as calculated by Aragon are also close to the ellipsoid line, and with $1<[\sigma]_{id}/[\sigma]_{pi}<1.01$, their $q_{\eta,id}$ values are probably all trustworthy. Therefore, the technique described here for inferring the intrinsic viscosity appears accurate for all ellipsoids, for all dumbbells having separation-to-diameter ratios below about 10, for cylinders with d/h in the range 0.1–0.4, as well as all five platonic solids.

VI. SUMMARY AND CONCLUSIONS

A previously developed technique [8–10] for determining the intrinsic viscosity of arbitrarily shaped bodies has been modified in this paper in two separate ways. The technique begins with a path integration to determine the polarizability tensor of a perfect conductor having the same size and shape as the body. The only source of uncertainty in this first step is sampling error in the path integration. The second step, inference of the intrinsic viscosity from the polarizability, generates greater uncertainty, and both modifications presented here address the problem of minimizing this uncertainty. Accompanying this procedure for the intrinsic viscosity is a parallel determination of the hydrodynamic radius which has always been more accurate and which is not being modified here.

The first modification concerns the correct way to infer the intrinsic viscosity within the framework of the Zimm rigid-body approximation [29], which involves performing averages over the conformational ensemble when the body is flexible. The correct approach is given by Eq. (10) or Eq. (21). In other words, it is not the polarizability itself that should be averaged over conformations, but intermediate quantities from which first, the polarizability, and then second, the intrinsic viscosity, are determined. We have already observed in work on the wormlike chain that Eq. (10) is more accurate than Eq. (9) [30].

The second modification is intended to improve the uncertainty in the estimate of the intrinsic viscosity of a single, rigid conformation. The previous approach was based on Eq. (16) for the ratio q_η, which is universally true for all shapes and does not reflect the shape dependence of q_η. However, we have conjectured that much of this shape dependence can be obtained from the full polarizability tensor. We have developed the Padé approximant given in Eqs. (19) and (20) that determines q_η for an arbitrary ellipsoid from the eigenvalues of the polarizability tensor of the ellipsoid. The assumption then is that any body that possesses the same polarizability tensor as some particular ellipsoid will also have a q_η value close to that of the ellipsoid. Therefore the approach is (apart from the fitting error in the Padé approximant) exact for ellipsoids. It also appears to work very well for dumbbells if they are not too widely separated. Beyond these two classifications of shapes, all additional comparisons must be made against finite-element results for $[\eta]$, which can be unreliable because of slow convergence. However, our approach lets us independently check the reliability of the finite-element calculations by comparing predictions for $[\sigma]$. Based on such a comparison, we are able to place considerable confidence in the AH [18] calculation on the platonic solids and on Aragon's results [39] for cylinders, and these agree to within 1.5% with the technique we have developed. Therefore it appears that the intrinsic viscosity of all five platonic solids and of cylinders with d/h in the interval 0.1–0.4 can also be inferred accurately by this approach.

The DG finite-element calculations [3] on a number of different shapes do not give such good agreement for $[\sigma]$, and probably reflect a larger error. (This point is appreciated and discussed by Douglas and Garboczi [3].) They also do not agree as well with our predictions for q_η, and, in fact, deviate systematically by about −2%. If we apply a ca. +2% correction to the DG data, then they agree very well with our results, and the uncertainty in q_η as predicted by our approach falls to about 1.5%. The same correction must be applied to obtain agreement between the DG and the AH results for the cube. In summary, if it proves that the DG data are indeed subject to the ca. −2% systematic error, then our approach gives 1.5% or less uncertainty in the determination of $[\eta]$, at least for all shapes considered. If the DG data prove to be more accurate, then the uncertainty of this approach could be as large as about 2% to 3%. Either way, this is an improvement over the 5% uncertainty that has existed up until this point. Furthermore, we have obtained this improved level of accuracy for *all* available exact or accurate numerical computations. We obviously have no guarantee that other shapes will give this same level of uncertainty, but it is significant that it affords an improvement in every case for which comparisons are possible.

Our improved method of estimating the intrinsic viscosity, when combined with our estimate of the hydrodynamic radius, is expected to be a powerful tool in the characterization of nanoparticles and biological macromolecules. The enhanced accuracy should allow more precise estimates of the structure of these particles based on transport property measurements, and we look forward to developing our method for applications of this kind.

ACKNOWLEDGMENTS

We are grateful to Sergio Aragon of San Francisco State University for providing boundary-element results on cylinders prior to publication. Computational support of the High Performance Computing Facility at Stevens Institute of Technology is also acknowledged.

APPENDIX: MOTIVATION FOR THE FORM OF EQ. (19)

Note that the Padé approximant depends on x_1 explicitly through e^{x_1}, but that it depends directly on x_2. It is well-known that for quasi-one-dimensional bodies, both electrostatic and hydrodynamic properties depend on the logarithm of the aspect ratio, while for quasi-two-dimensional bodies, they depend on the aspect ratio itself. Therefore terms in e^{x_1} and in x_2 were used under the assumption that such forms would permit the approximant to more faithfully represent the function as the respective limits are approached. We have also constructed it to reproduce the following known limits [3]:

$$q_\eta(0,0) = \frac{5}{6}, \tag{A1}$$

$$q_\eta(x_1,\infty) = \frac{4}{5}, \tag{A2}$$

$$q_\eta(\infty,0) = \frac{4}{5}. \tag{A3}$$

By direct observation of the computed results, it is apparent that

$$\left| \frac{\partial q_\eta}{\partial x_2} \right|_{x_2=0} = 0 \tag{A4}$$

and this condition is also incorporated into our approximant.

---

[1] H. Yamakawa, *Modern Theory of Polymer Solutions* (*Harper & Row*, New York, 1971).

[2] J. B. Hubbard and J. F. Douglas, Phys. Rev. E **47**, R2983 (1993).

[3] J. F. Douglas and E. J. Garboczi, Adv. Chem. Phys. **91**, 85 (1995).

[4] E. J. Garboczi and J. F. Douglas, Phys. Rev. E **53**, 6169 (1996).

[5] H.-X. Zhou, A. Szabo, J. F. Douglas, and J. B. Hubbard, J. Chem. Phys. **100**, 3821 (1994).

[6] J. F. Douglas, H.-X. Zhou, and J. B. Hubbard, Phys. Rev. E **49**, 5319 (1994).

[7] J. A. Given, J. B. Hubbard, and J. F. Douglas, J. Chem. Phys. **106**, 3761 (1997).

[8] M. L. Mansfield, J. F. Douglas, and E. J. Garboczi, Phys. Rev. E **64**, 061401 (2001).

[9] M. L. Mansfield and J. F. Douglas, Condens. Matter Phys. **5**, 249 (2002).

[10] E.-H. Kang, M. L. Mansfield, and J. F. Douglas, Phys. Rev. E **69**, 031918 (2004).

[11] J. F. Douglas, Adv. Chem. Phys. **102**, 121 (1997).

[12] S. Haber and H. Brenner, J. Colloid Interface Sci. **97**, 496 (1984).

[13] G. K. Youngren and A. Acrivos, J. Fluid Mech. **69**, 377 (1975).

[14] D. Brune and S. Kim, Proc. Natl. Acad. Sci. U.S.A. **90**, 3835 (1993).

[15] S. A. Allison, Macromolecules **32**, 5304 (1999).

[16] H. Zhao and A. J. Pearlstein, Phys. Fluids **14**, 2376 (2002).

[17] S. Aragon, J. Comput. Chem. **25**, 1191 (2004).

[18] S. R. Aragon and D. K. Hahn, J. Chem. Theory Comput. **2**, 12 (2006).

[19] D. K. Hahn and S. R. Aragon, J. Chem. Theory Comput. **2**, 1416 (2006).

[20] J. Garcia de la Torre and V. A. Bloomfield, Q. Rev. Biophys. **14**, 81 (1981).

[21] J. Garcia de la Torre, S. Navarro, M. C. Lopez Martinez, F. G. Diaz, and J. J. Lopez Cascales, Biophys. J. **67**, 530 (1994).

[22] J. Garcia de la Torre and B. Carrasco, Eur. Biophys. J. **27**, 549 (1998).

[23] B. Carrasco and J. Garcia de la Torre, Biophys. J. **75**, 3044 (1999).

[24] B. Carrasco and J. Garcia de la Torre, J. Chem. Phys. **111**, 4817 (1999).

[25] J. Garcia de la Torre, M. L. Huertas, and B. Carrasco, Biophys. J. **78**, 719 (2000).

[26] J. Garcia de la Torre, O. Llorca, J. L. Carrascosa, and J. M. Valpuesta, Eur. Biophys. J. **30**, 457 (2001).

[27] J. Garcia de la Torre and B. Carrasco, Biopolymers **63**, 163 (2002).

[28] J. Garcia de la Torre, G. del Rio Echenique, and A. Ortega, J. Phys. Chem. B **111**, 955 (2007).

[29] B. H. Zimm, Macromolecules **13**, 592 (1980).

[30] M. L. Mansfield and J. F. Douglas, Macromolecules **41**, 5412 (2008); **41**, 5422 (2008).

[31] In previous work on ideal random-coil chains, we naively employed Eq. (9) rather than Eq. (10) [9]. We plan to revisit this question in an extensive work on the intrinsic viscosity of random coils in the near future.

[32] F. Perrin, J. Phys. Radium **7**, 1 (1936).

[33] Based on an integral equation formulation, Zhou [H.-X. Zhou, Biophys. J. **69**, 2286 (1995)] and Aragon and Hahn [18] have proposed $q_\eta = 3/4$, but this lies in the lower range of the interval of Eq. (16).

[34] It is well-known than an ellipsoid is a very useful geometrical representation of any second-rank positive-definite symmetric tensor. The physical ellipsoid whose hydrodynamic and electrostatic properties are under consideration is equivalent to the tensor

$$\begin{bmatrix} a_1 & 0 & 0 \\ 0 & a_2 & 0 \\ 0 & 0 & a_3 \end{bmatrix}.$$

The "polarizability ellipsoid," on the other hand is an abstract representation of the polarizability tensor,

$$\begin{bmatrix} \alpha_1 & 0 & 0 \\ 0 & \alpha_2 & 0 \\ 0 & 0 & \alpha_3 \end{bmatrix},$$

and is therefore distinct from the physical ellipsoid. However, both ellipsoids have the same principle axes and belong to the same symmetry group. The coordinates (x_1,x_2), defined in Eq.

(17a) and (17b) and generating our shape space, refer to the shape of the polarizability ellipsoid, while the coordinates (z_1,z_2) describe the shape of the physical ellipsoid.

[35] Although the polarizability tensor of any arbitrary object is symmetric, the tensor as determined by path integration can be slightly asymmetric due to sampling error and therefore can have complex eigenvalues. Prior to diagonalization, we recommend symmetrizing the polarizability tensor by replacing it with $\frac{1}{2}(\boldsymbol{\alpha}+\boldsymbol{\alpha}^T)$.

[36] S. Wakiya, J. Phys. Soc. Jpn. **31**, 1581 (1971); **33**, 278(E) (1972).

[37] H. Brenner, Int. J. Multiphase Flow **1**, 195 (1974).

[38] All but two of the points for dumbbells lie close to the line for ellipsoids. The departure of the (1.128)-dumbbell must be due to an error in the reported data, since this point also deviates from the trend set by the dumbbell points on either side. The $(r_p=\infty)$-dumbbell also departs from the ellipsoid line, but we regard this as accurate. Somewhere beyond $r_p \approx 10$, this approach becomes inappropriate for dumbbells and is unable to match their behavior as $r_p \to \infty$.

[39] S. Aragon (private communication).

[40] The sphere as well as any bodies belonging to the symmetry groups T_d, O_h, and I_h have three degenerate eigenvalues: $\alpha_1 = \alpha_2 = \alpha_3$, which indicates that $q_{\eta,\mathrm{Pade}} = 5/6$ for all such bodies. This includes all of the platonic solids, as well as a few other bodies listed in Table II.